A comprehensive analysis of the Illapel 2015 Mw 8.3 Earthquake from GPS and InSAR data.
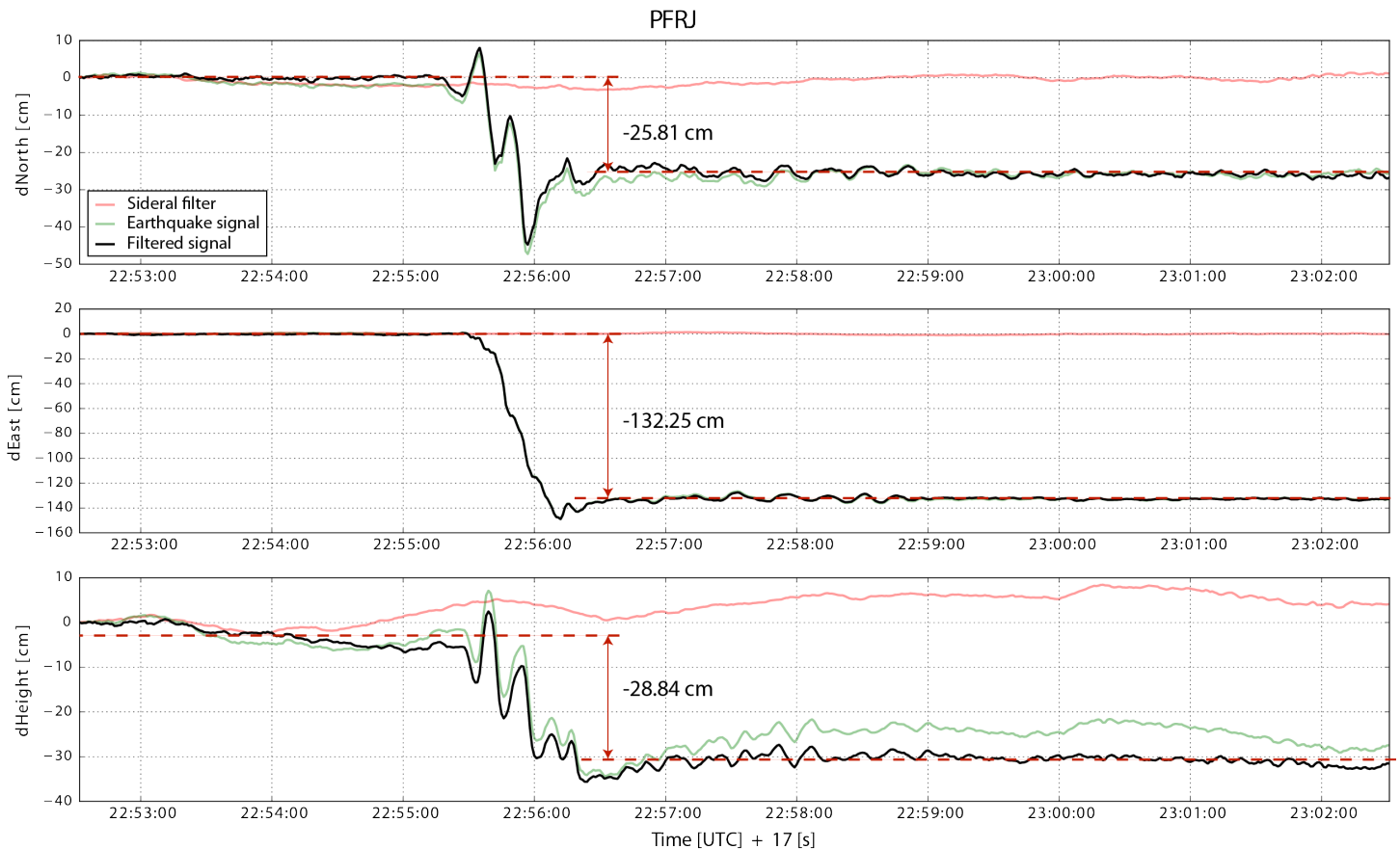
Klein, E.[1][2], Vigny, C.[1], Fleitout, L.[1], Grandin, R.[3], Jolivet, R.[1], Rivera, E.[4], Métois, M.[5]

5

Supplementary material

GPS Data
High rate GPS data processing

Figure S1: Motogram of station Parque Frey Jorge (PFRJ) : green curve : original signal, red curve : sideral filter, black curve : filtered signal. The red arrows shows the estimation of static coseismic offset on the filtered motogram

Static GPS processing. 24 hr sessions are reduced to daily site positions using the GAMIT software [King & Bock 2000]. We choose the ionosphere-free combination, with fixed ambiguities to integer values. Precise orbits from the International GNSS Service for Geodynamics [IGS; Dow et al. 2009] are used together with the description from IGS tables of the phase centres of the antennae. We estimate one tropospheric vertical delay parameter per station every 3 hr. The horizontal (resp. vertical) components of the calculated relative position vectors have repeatabilities of 1–3 (resp. 3–5) mm. Daily time-series are then produced using the GLOBK software [Herring et al. 2010]. In order to deal with the large scale postseismic deformation following the Maule earthquake [Klein et al., 2016], we combine our daily solutions with daily global H-files produced at SOPAC, using

globally distributed IGS stations. We produce daily coordinates, mapped into the ITRF 2008 (Altamimi et al. 2011) using a set of regional and global stations with well-known coordinates in the ITRF08 [the reference frame can be found in Klein et al., 2016]. Residuals are typically of the order of 3–5 mm, indicating the level of precision of the mapping in the ITRF.

Figure S2: Campaign time series of the site ESAU showing the process of coseismic estimation

Figure S3: Co-seismic static displacement field for survey sites (at +15 to 30 days after the earthquake) on the horizontal (left) and vertical (right) components. Ellipses depict the 95% confidence level of formal uncertainties. The yellow star highlights the main shock epicenter, the red one, the strongest aftershock (CSN).

sGPS uncertainties estimation. The uncertainties are defined as $\sigma_{co} = \sqrt{\sigma_{extP}^2 + \sigma_{inter}^2}$ (S1)

with σ_{extP} the uncertainty on the post-earthquake position, and σ_{inter} defined as

$$\sigma_{inter} = \sqrt{\frac{\sum (\tilde{x}_i - x_i)^2}{n}} \quad \text{(S2)}$$

60 where x_i are the campaign positions before the earthquake on which the interseismic velocity is interpolated, $\tilde{x}_i$ the positions predicted at the campaign date by the estimated interseismic velocity, and n the number of measurements used to estimate the interseismic velocity (fig.S2).
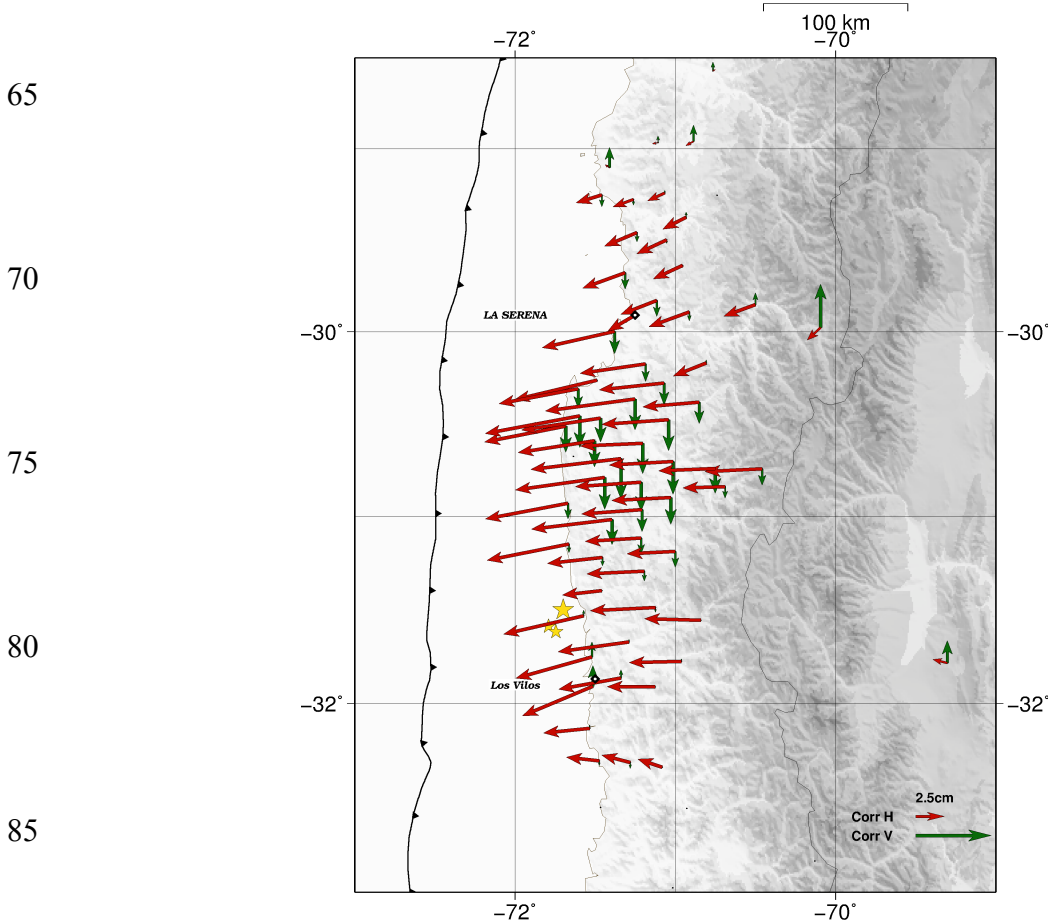
Figure S4: Correction applied on survey sites horizontal (red arrows), and vertical (green arrows) to extract the purely coseismic deformation.

90 Note that vertical displacements measured by GPS are affected by a very large scale signal that has probably not a tectonic origin, producing 8mm of uplift on the whole network during the considered period. Therefore raw measurements are corrected from this drift fixing a null vertical displacement for the stations furthest from the trench.

95

100
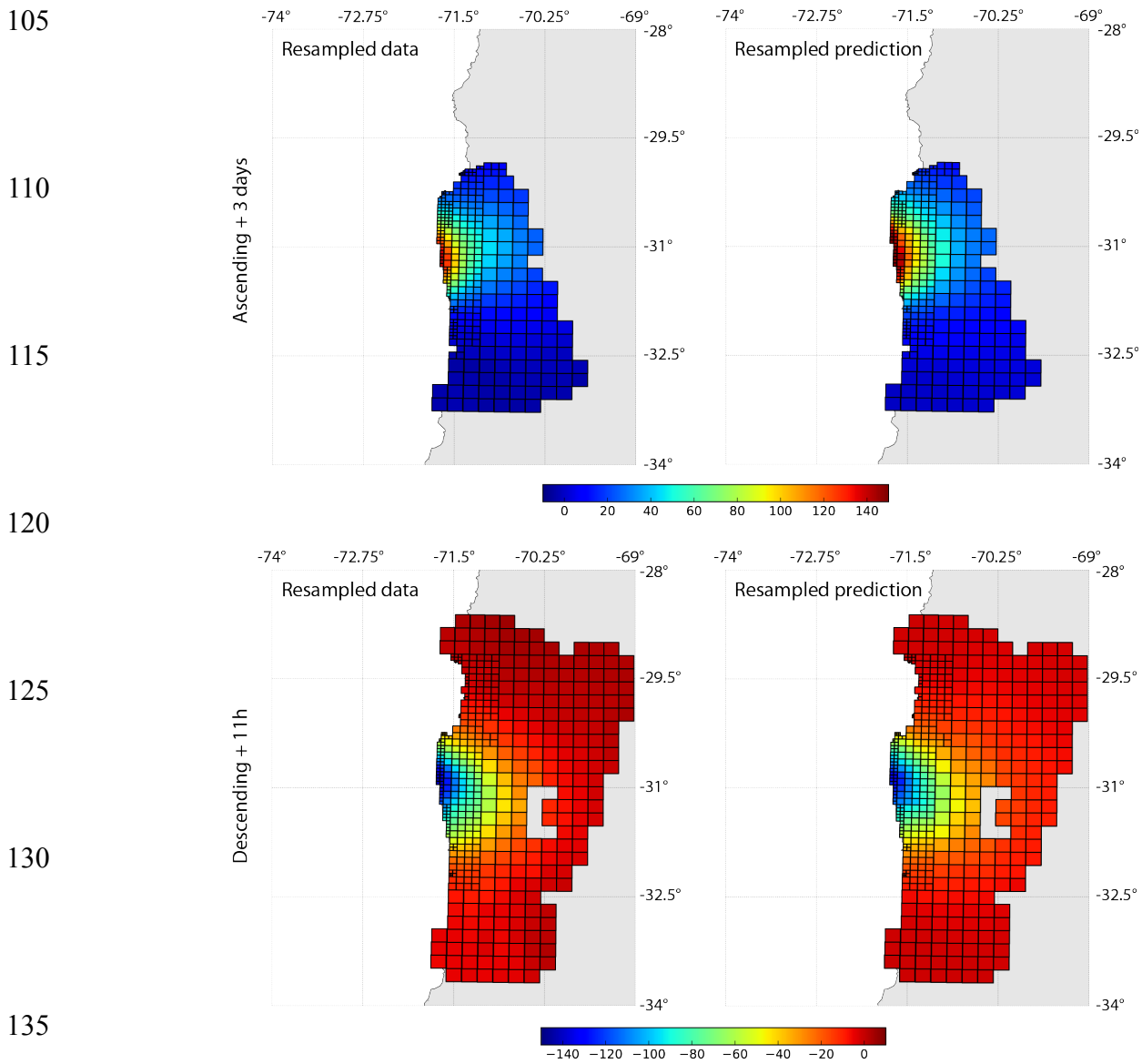
Figure S5: Resampled INSAR interferograms for ascending and descending tracks vs interferograms predicted by the preferred model.
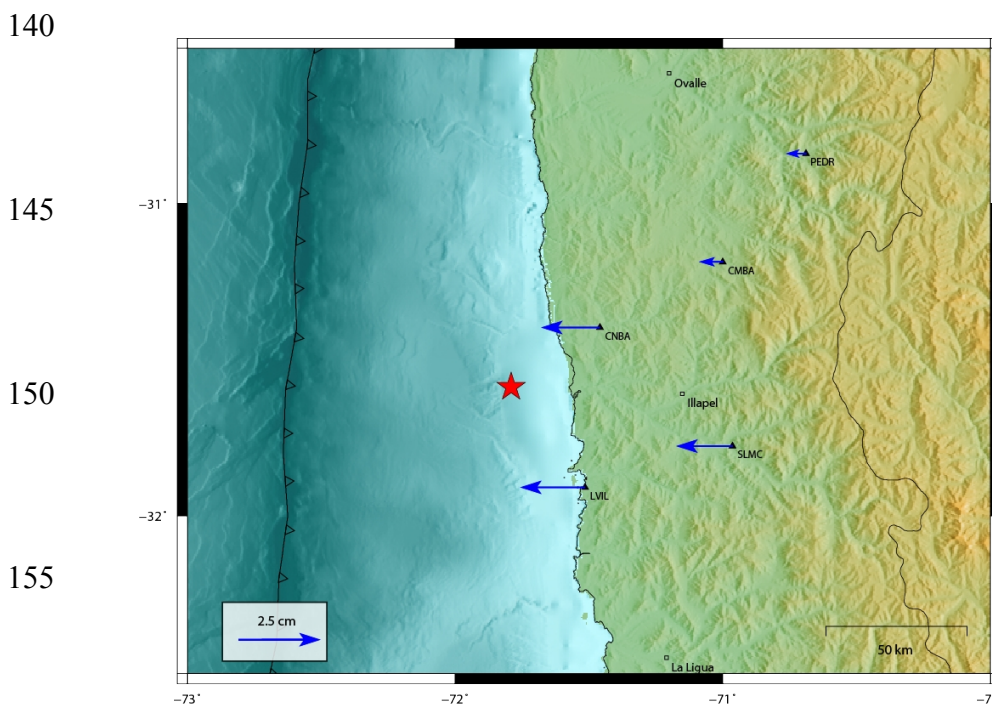
Figure S6a: Static coseismic displacement field of the main aftershock on the east component (in cm) only, the north component could not reliably be extracted from motograms because too small compared to the noise. The red star depicts the location of the epicenter.
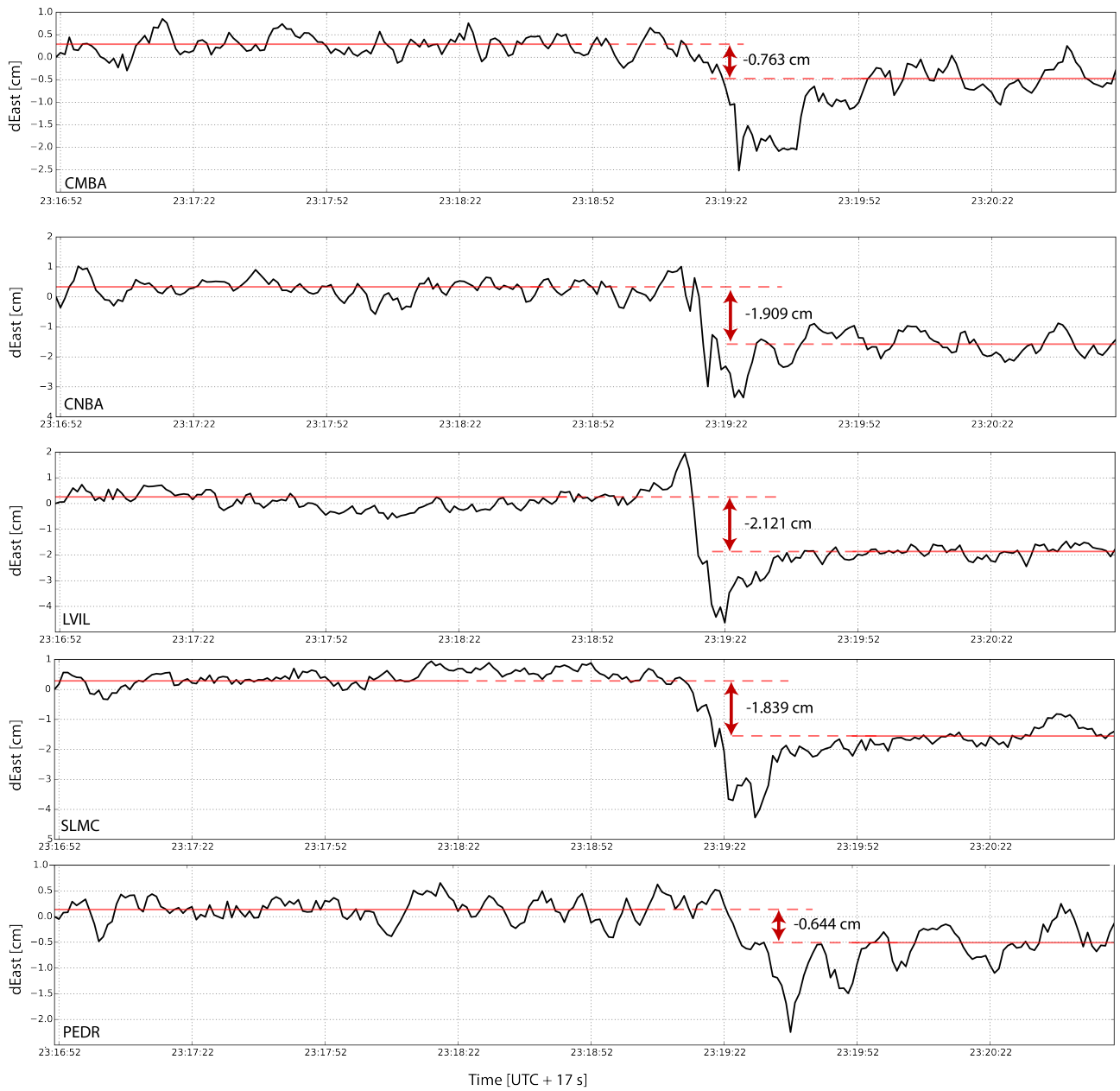
160 **Figure S6b:** Motograms (East component) of the 5 cGPS stations that recorded the main aftershock, used to estimate the static offset (Fig S6a).
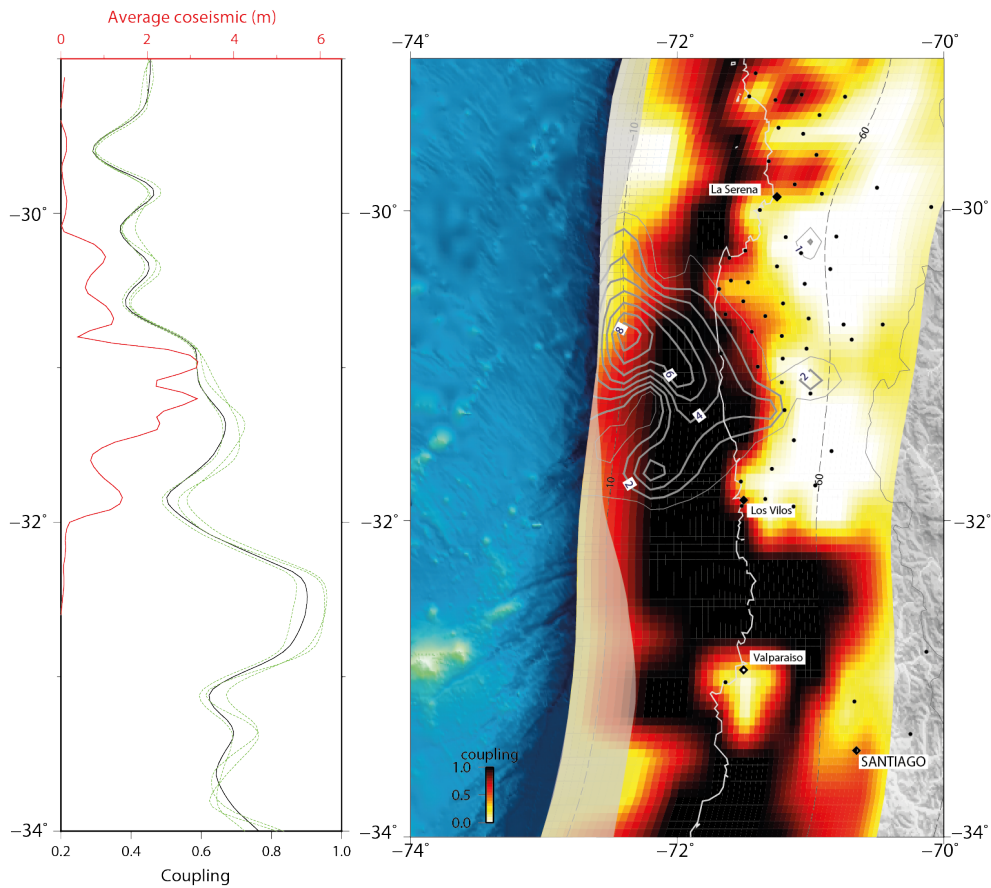
Figure S7: Average coseismic slip amount for the best model (red curve also represented with grey 1m contours on the map) compared to along-strike variations of the average coupling value from the trench to 60 km depth (black curve, also represented on the map) and three alternative models that fit almost equally well with the data (different smoothing parameters, green dashed curves) [Métois et al., 2016].
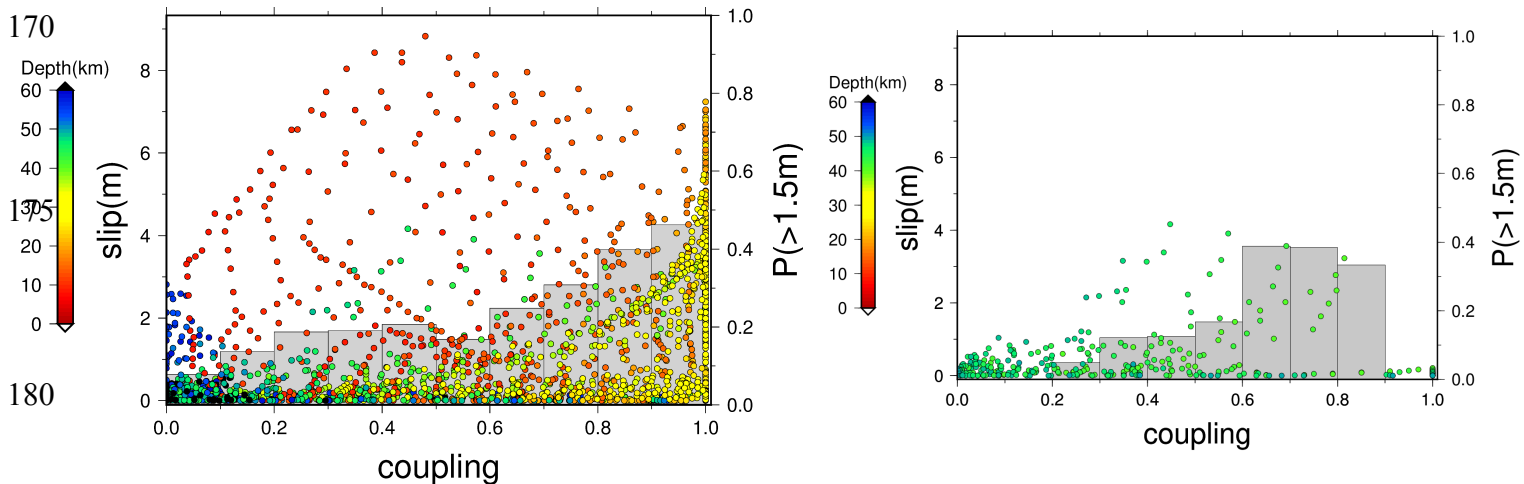
Figure S8: Correlation between coseismic slip amount from the best model presented in fig. 4 and prevailing interseismic coupling from [Métois et al., 2016] (left: for all patches of the interface; right) for patches located between 40 and 50 km depth). Each subfault is represented by dots color coded depending on its depth, coseismic slip during the Illapel earthquake and interseismic coupling value. Overall, the amount of coseismic slip is higher for higher coupling values. Outsiders to this tendency are mainly very shallow subfaults where resolution is low both on the co-seismic and coupling models (also because it is not clear at which point shallow fault portions require to be coupled to slip co-seismically [e.g. Cubas et al., 2013]). We also observe a strong decorrelation on some patches showing a high coupling value (>0.9) that did not slip coseismically. They remain marginal and could be artifacts from the coupling model, placed at depth to reproduce local velocity anomalies.
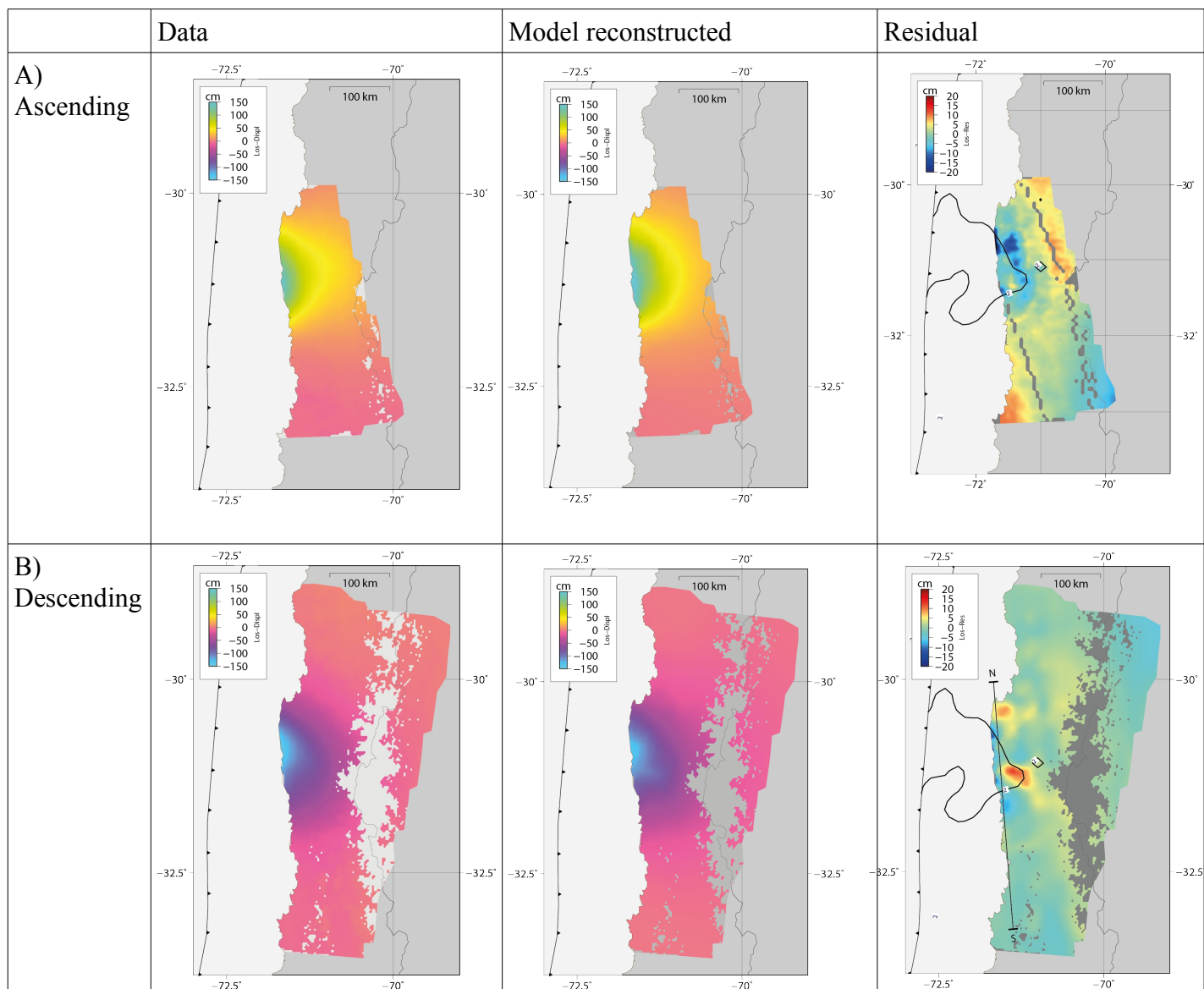
The conditional probability of experiencing more than 1.5m of coseismic slip depending on the prevailing coupling amount, $P_{.>1.5m/coupling}$ is represented by gray histograms (equation given

below, for more details, refer to [Métois et al.,2016]). The correlation coefficient R2 between $P_{.>1.5\text{m}/coupling}$ and the interseismic coupling is of 0.87.

$$P_{.>1.5\text{m}/coupling} = \frac{N_{subfaults_{.>1.5\text{m}/coupling}}}{N_{subfaults_{coupling}}} \quad \text{(S3)}$$

200

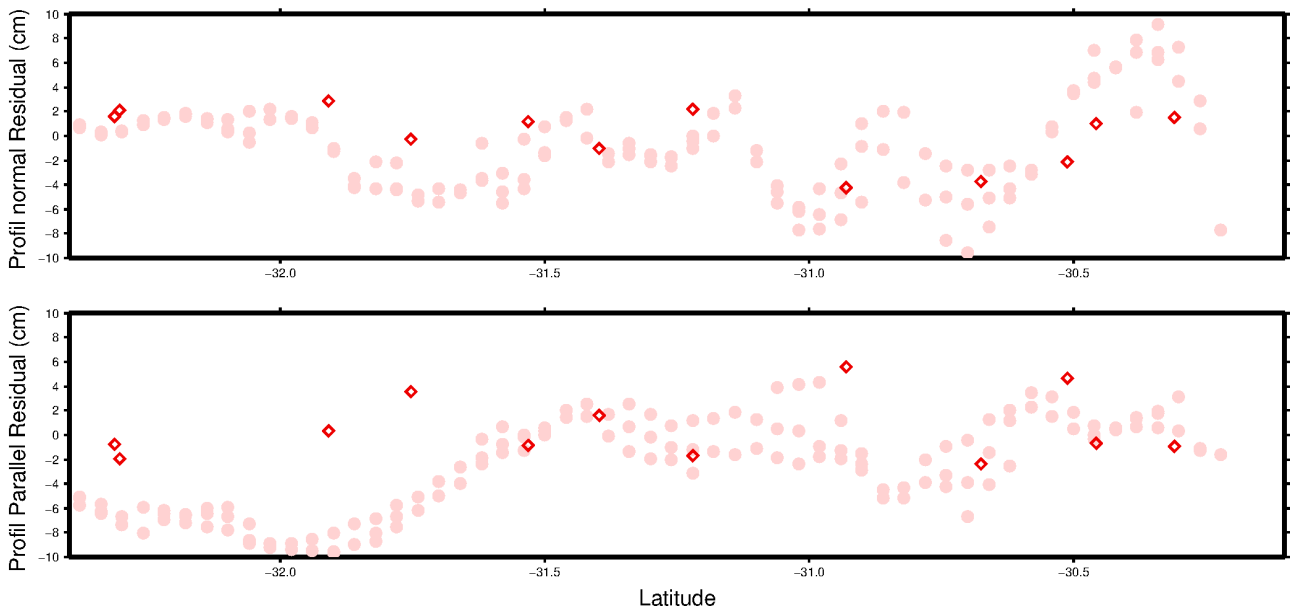|	Data	Model reconstructed	Residual
A) Ascending			
B) Descending			

Figure S9: Reconstructed unwrapped InSAR tracks (A) ascending and B) descending), prediction of the best fit model and residuals (observations – model)

205

210

Figure S10: Profil-normal and profil-parallel residuals of InSAR (pink dots) and GPS (red diamonds) residuals (obs – mod) of the preferred best fit model along a North-South profile (represented on fig.S10B-residuals)
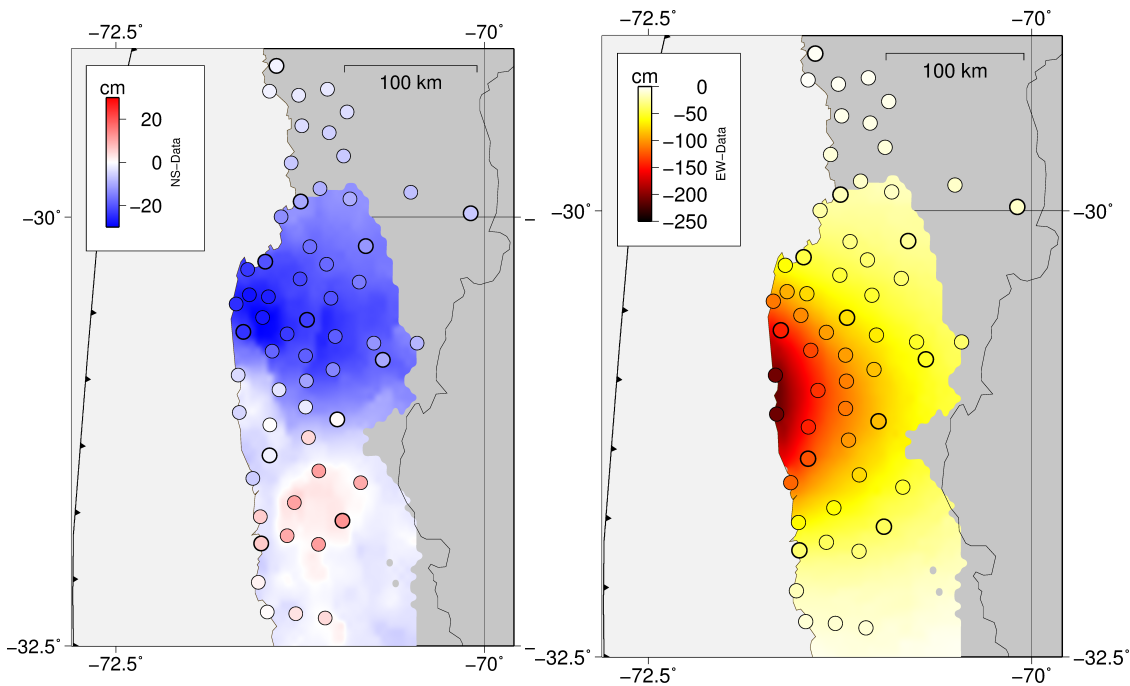
Figure S11: Horizontal coseismic displacements NS (left), EW (right) reconstructed from Sentinel-1 InSAR [Grandin et al.,2016] compared to GPS coseismic offsets. cGPS stations are depicted by darker contours.
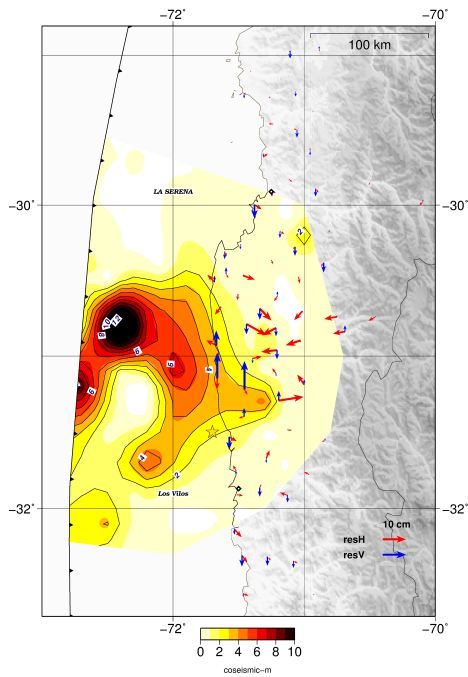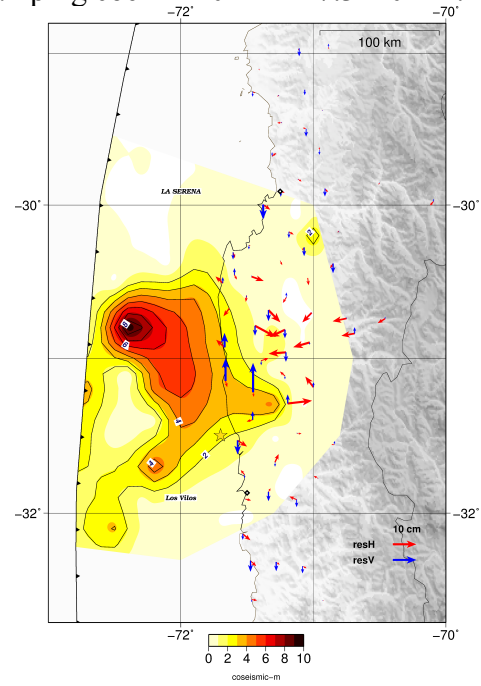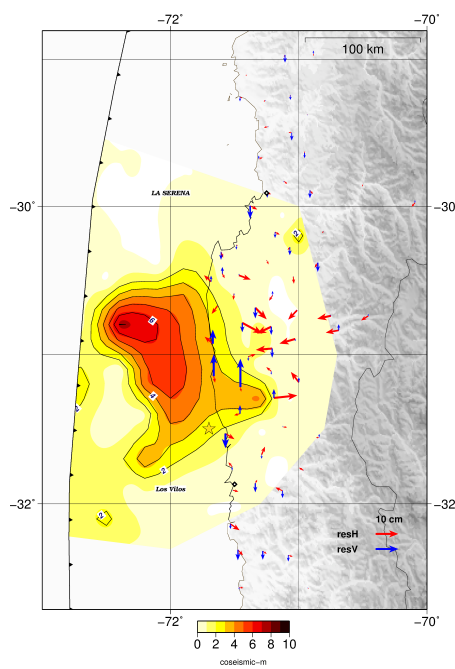
Damping effect
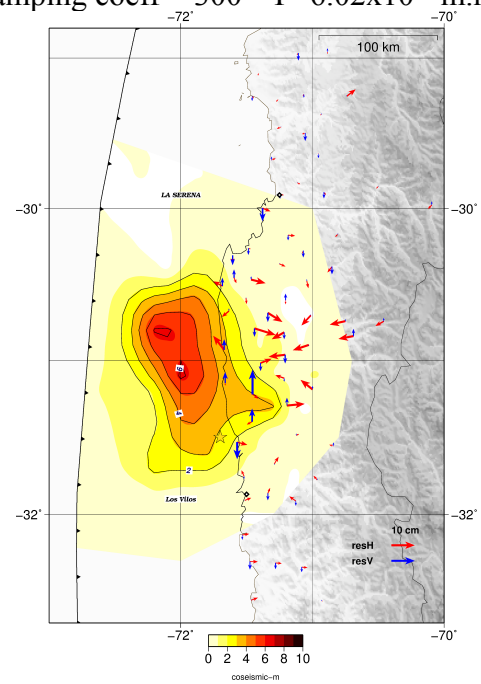
Figure S12: Residuals (Observations − model, red arrow for the horizontal component and blue arrows for the vertical component) for models inverted using different damping values (a) 10, b) 20, c) 30, d) 300) corresponding to an increasing importance of the damping in the penalty function as described in table 1 in the main text. Rake angle is left free. The corresponding coseismic slip distribution is represented in red color scale. The potency (geometrical moment) is given in each case.
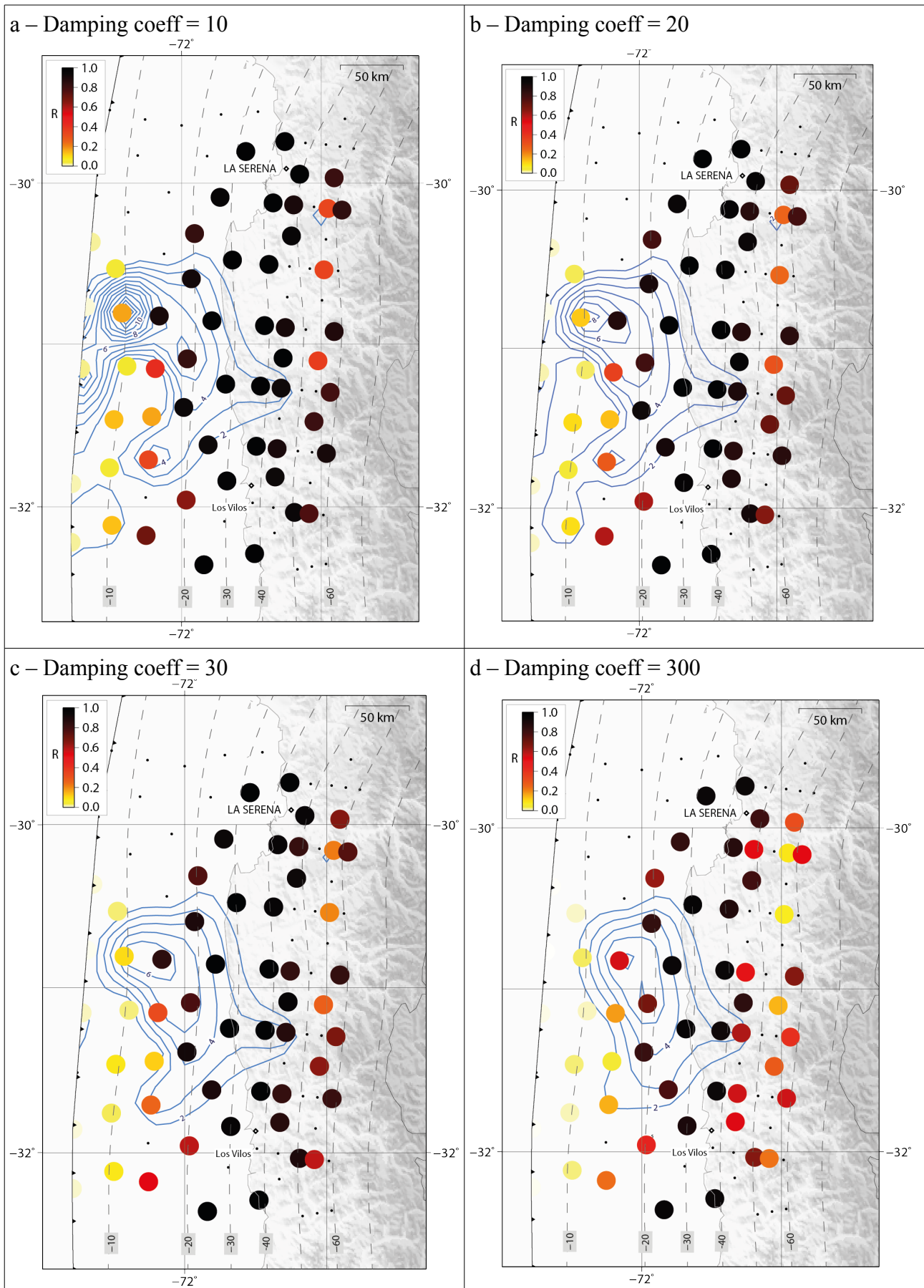
Figure S13: Diagonal terms of the Model resolution in each of the 4 cases with different damping values (presented on Fig.S12). The resolution is defined as:

$$R = G_s^{-1}.G = (G^t.C_d^{-1}.G + D_a.Id)^{-1}.G^t.C_d^{-1}.G \quad (S4) \text{ with } \quad G_s^{-1} \text{ the matrix relating the inverted}$$

model to the data: $\quad m = G_s^{-1}.d \quad , \quad D_a$ the damping coefficient and $\quad Id$ the identity matrix

250 [Dufumier & Rivera 1997; Tarantola 2005]. Note that R, being data and model dependent, will be equal to the identity matrix for $\quad D_a = 0$.

Moment estimation and seismic moment vs geodetic moment comparisons. With heterogeneous elastic parameters on both sides of the fault plane (our case), the calculation of the seismic moment is not as direct as in an homogeneous half space (most previous studies). We follow here two different methodologies to estimate a seismic moment that can be compared with other studies. The first method is 3-steps: First, we estimate the potency distribution, which is independent of the geometry. Then, this potency distribution is re-injected in a PREM distribution, homogeneous on both sides of the fault. And finally, we estimate the seismic moment in this PREM distribution, which makes it comparable with seismological studies. The second method is more straightforward: we compute the seismic moment using an effective shear modulus defined following [Wu & Chen, 2003] and [Vavrycuk et al., 2013] by :

$$\mu' = 2 \ (\ \mu^+ . \mu^- \ / \ (\mu^+ + \mu^-)) \qquad (S5)$$

with μ^+ and μ^- the shear moduli of both sides of the fault. Seismic moments calculated using both methodologies are very close (within 10%) (Table S1). Allowing the slip vector to vary or constraining it to the plate convergence direction does not change the seismic moment significantly either. The largest variations depend on the damping factor: almost 30% between the lowest and the highest estimates. Note that a contribution of some 2.0×10^{20}N.m., corresponding to earthquakes and slip during the first day should be added to the seismological estimate before comparison with the values from table 2. All are in the range of the seismological estimate.

|	Damping variation	P (m.m²)	'Effective' distribution		PREM distribution	
			M_0 (N.m)	Mw	M_0 (N.m)	Mw
free rake	cm10	8.20E+010	3.56E+021	8.30	3.55E+021	8.30
	cm20	7.31E+010	3.24E+021	8.27	3.35E+021	8.28
	cm30	6.73E+010	3.04E+021	8.26	3.25E+021	8.27
	cm300	6.02E+010	2.80E+021	8.23	3.09E+021	8.26
fixed rake	cm20	8.25E+010	3.58E+021	8.30	3.53E+021	8.30
	Preferred mod (cm30)	7.68E+010	3.38E+021	8.29	3.42E+021	8.29

Table S1: *Potency, Seismic moment and Magnitude estimated with the 2 methodologies, for 6 models with different damping value, with rake 'fixed' or 'free', to be compared with W-phase estimation: $M_0 = 3.19 \times 10^{21}$ N.m (Mw8.3) and Global CMT estimation : $M_0=3.23 \times 10^{21}$ N.m (Mw8.3).*

Shallow slip or not - Sensitivity study
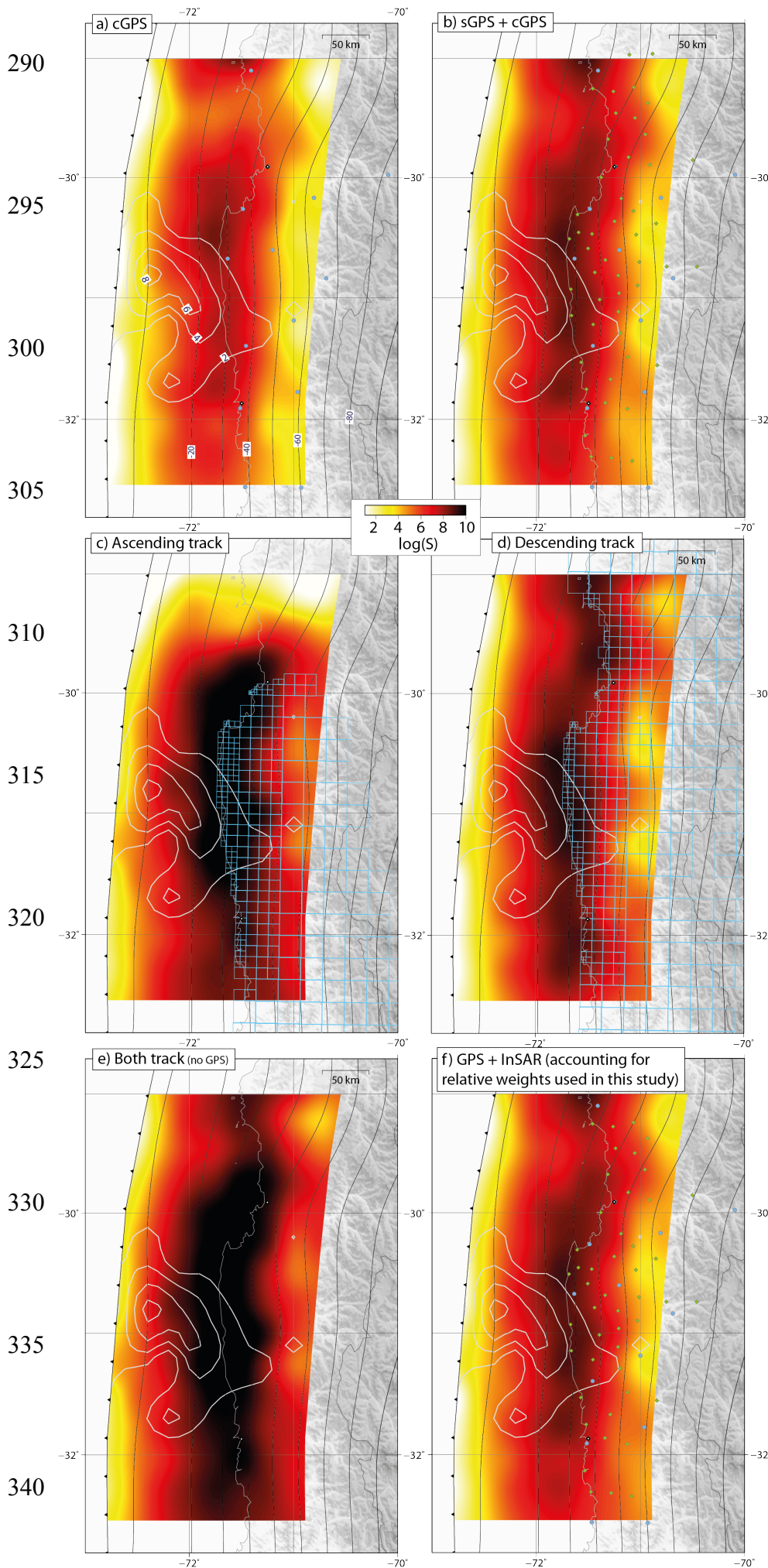
Figure S14: Sensitivity (defined in equation (2)) maps for different datasets. The covariance matrix Cd is a diagonal matrix of the uncertainties for the GPS data, and a non-diagonal matrix for InSAR data (details in the main text, [Jolivet et al., 2015].
a) cGPS only ;
b) cGPS + sGPS ;
c) InSAR ascending ;
d) InSAR descending ;
e) Two InSAR tracks ;
f) cGPS+ sGPS + InSAR.
Blue dots represent continuous GPS stations, green diamons campaigns sites, blue square contours represent resampled squares of InSAR. The 2 m contours of the preferred coseismic model are represented in white. The 10 km-isolines from Slab1.0 are represented in black.
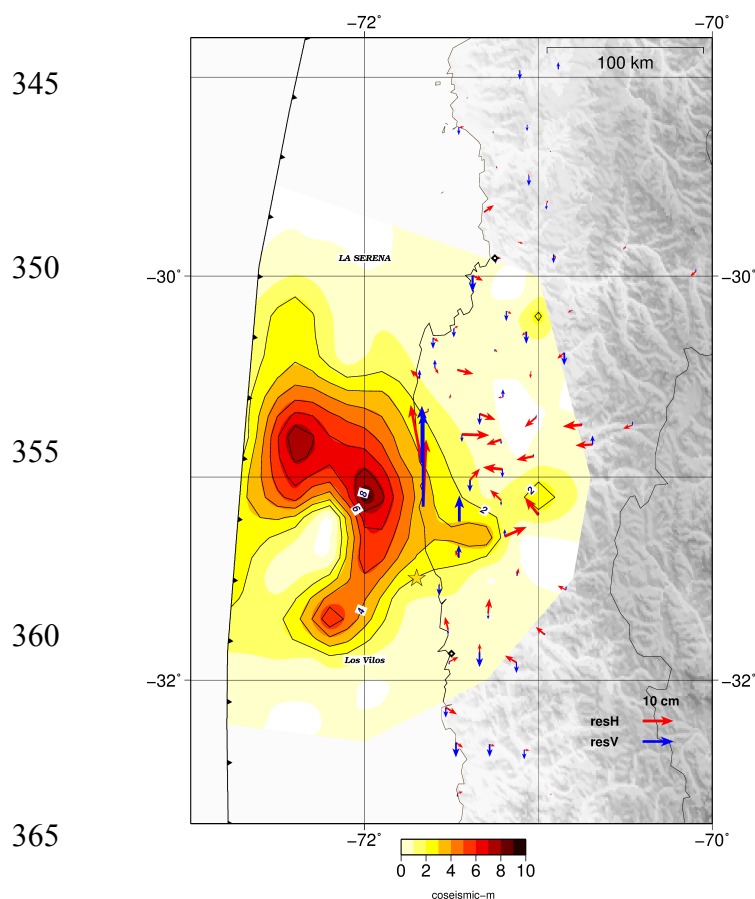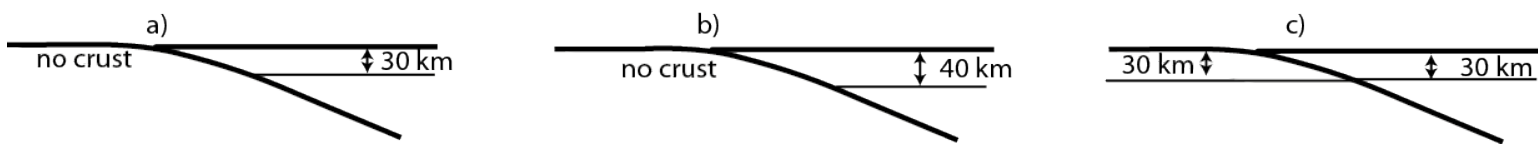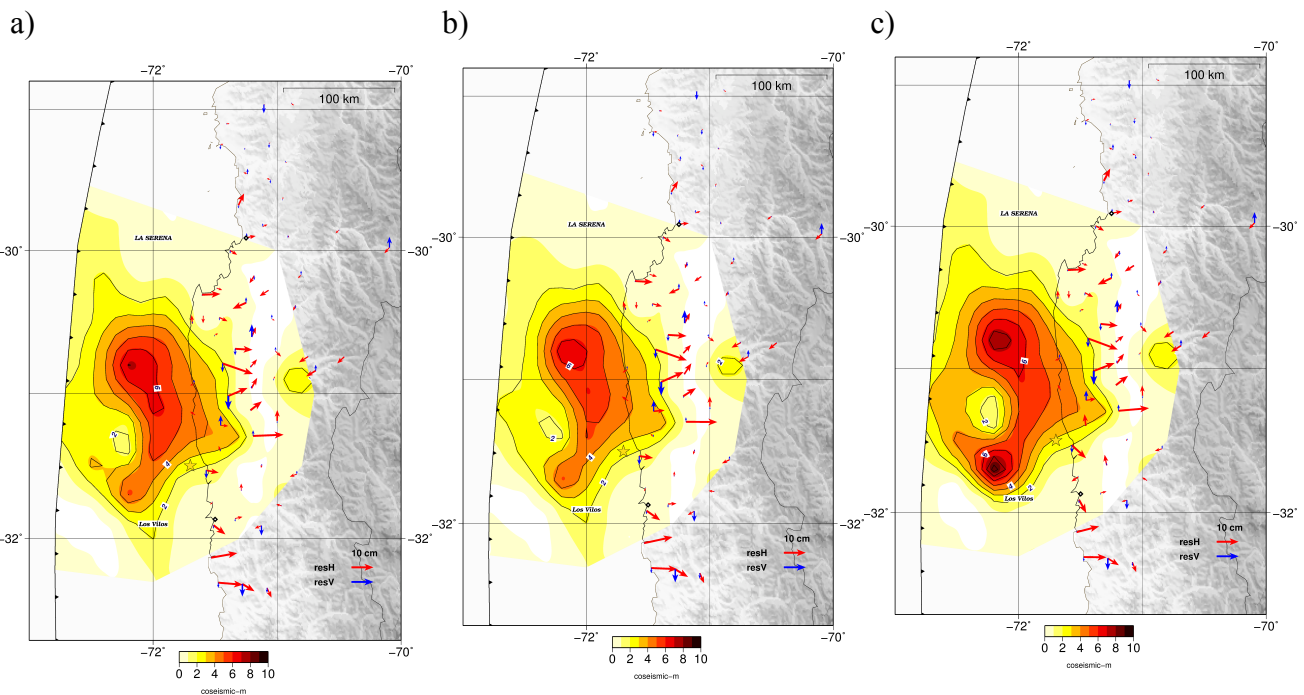
Figure S15: Inverted coseismic slip distribution without using the data from stations EMAT and CTAL located at the coast which have the maximum horizontal offsets. Arrows represent the residuals (red in horizontal, blue in vertical)

Geometry effect. The exact elastic moduli in the overriding and subducting plates and the thickness of the crust are poorly known, in particular on the shallowest part of the subduction interface. Seismic refraction studies have been conducted in North Chile (CINCA experiment) and in South Chile, focused on the Arauco Peninsula (SPOC experiment), but not in the region of the Illapel earthquake. There, a transition between erosive and accretionnary regime is proposed, supposedly due to morphologic changes of the oceanic plate [Oncken et al., 2006]. But precise evidences are sparse and the value of shear moduli remains unconstrained. Moreover, models of coseismic displacements very often involve a layered structure with similar crusts for the oceanic and continental crusts. Here, we simply test the impact of different geometries and elastic moduli of the subducting and overridding plates. In these tests, the damping coefficient is fixed to 100 and the rake angle is left free, so that geometry is the only varying parameter. We compare the slip distributions inverted with a 30 km thick continental crust and no oceanic crust (our preferred model – figS16-a); with a 40 km thick continental crust and no oceanic crust (fig.S16-b) and with equal parameters (30 km - thick crust) on both sides of the fault (fig S16-c). The slip amplitude varies and is the strongest in the case of the homogeneous geometry, as expected: the artificial low moduli in the oceanic lithosphere favor stronger displacements below the subduction interface. Slip amplitude is also slightly stronger in the case of the 30 km-thick continental crust. We note that the potencies differ by 19% and the M_0 by 14% between the case with a 40km thick crust (b) and the

case with equal parameters on both sides (c) (table S2 in the supplementary material). This has to be compared with the spread of potencies and moments in table 2 which is similar. One should thus keep in mind that differences below 20% between the seismic moment deduced from seismology or from GPS and InSAR displacements could be due to errors in the elastic structure as well as to an inappropriate choice of the regularization parameters in the inversion. Note also that the widespread choice of a layered structure for the modeling of coseismic displacements significantly enhances the predicted moment.

	Case	Potency (m.m^2)	M_0 (PREM) (N.m)
a)	Crust 30 km	8.63x10^{10}	4.0831x10^{21}
b)	Crust 40 km	7.97x10^{10}	3.844x10^{21}
c)	Uniform Crust	9.51x10^{10}	4.3961x10^{21}

Table S2: Estimated potencies and seismic moment for each models.

Figure S16: Effect of crust on coseismic slip distribution :
a) standard crust (continental crust 30 km – thick, no oceanic crust) ; b) thicker crust (continental crust 40 km – thick, no oceanic crust) ; c) uniform geometry (30 km - thick crust on both oceanic and continental crust). In the 3 cases, inversions are made with GPS data only, with rake 'free' and damping of 100. Arrows represent the residuals (red in horizontal, blue in vertical)

Supplementary references

Altamimi, Z., Collilieux, X., & Métivier, L. (2011). ITRF2008: an improved solution of the international terrestrial reference frame. *Journal of Geodesy*, *85*(8), 457-473.

Cubas, N., Avouac, J. P., Leroy, Y. M., & Pons, A. (2013). Low friction along the high slip patch of the 2011 Mw 9.0 Tohoku-Oki earthquake required from the wedge structure and extensional splay faults. Geophysical Research Letters, 40(16), 4231-4237.

Dow, J., Neilan, R., Rizos, C., The International GNSS Service in a changing landscape of Global Navigation Satellite Systems, Journal of Geodesy 83 (3- 4) (2009) 191–198. doi:10.1007/s00190-008-0300-3.

Dufumier, H., Rivera, L. On the resolution of the isotropic component in moment tensor inversion. *Geophys J Int* 1997; 131 (3): 595-606. doi: 10.1111/j.1365-246X.1997.tb06601.x

Grandin, R., Klein, E., Métois, M., & Vigny, C. (2016). Three-dimensional displacement field of the 2015 Mw8.3 Illapel earthquake (Chile) from across-and along-track Sentinel-1 TOPS interferometry. *Geophysical Research Letters*, *43*(6), 2552-2561.

Herring, T., King, R., and McClusky, S. C. (2010). GAMIT : GPS Analysis at MIT, release 10.4.

Herring, T., King, R., and McClusky, S. C. (2010). GLOBK : Global Kalman filter VLBI and GPS analysis program release 10.4.

Klein, E., Fleitout, L., Vigny, C., & Garaud, J. D. (2016). Afterslip and viscoelastic relaxation model inferred from the large-scale post-seismic deformation following the 2010 Mw 8.8 Maule earthquake (Chile). *Geophysical Journal International*, *205*(3), 1455-1472.

Métois, M., Vigny, C., & Socquet, A. (2016). Interseismic Coupling, Megathrust Earthquakes and Seismic Swarms Along the Chilean Subduction Zone (38°–18° S). *Pure and Applied Geophysics*, *173*(5), 1431-1449.

Oncken, O., Chong, G., Franz, G., Giese, P., Götze, H.-J., Ramos, V. A., Strecker, M. R., and Wigger, P. (2006). The Andes : active subduction orogeny. Springer Science & Business Media.

Tarantola, Albert. *Inverse problem theory and methods for model parameter estimation*. Society for Industrial and Applied Mathematics, 2005.

Vavryčuk, V. (2013). Is the seismic moment tensor ambiguous at a material interface?. *Geophysical*

Journal International, *194*(1), 395-400.

Wu, Z. L., & Chen, Y. T. (2003). Definition of seismic moment at a discontinuity interface. *Bulletin of the Seismological Society of America*, *93*(4), 1832-1834.